ANNUAL REVIEWS

Annual Review of Analytical Chemistry

Beginner's Guide to Micro- and Nanoscale Electrochemical Additive Manufacturing

Julian Hengsteler,[1] Karuna Aurel Kanes,[2] Liaisan Khasanova,[2] and Dmitry Momotenko[2]

[1]Laboratory of Biosensors and Bioelectronics, Institute for Biomedical Engineering, ETH Zurich, Zurich, Switzerland

[2]Department of Chemistry, Carl von Ossietzky University of Oldenburg, Oldenburg, Germany; email: dmitry.momotenko@uol.de

ANNUAL REVIEWS CONNECT

www.annualreviews.org

- Download figures
- Navigate cited references
- Keyword search
- Explore related articles
- Share via email or social media

Keywords

3D printing, electrodeposition, nanopipette, meniscus-confined electrodeposition, MCED, FluidFM, scanning ion conductance microscopy, SICM, electrohydrodynamic redox printing, EHD-RP

Abstract

Electrochemical additive manufacturing is an advanced microfabrication technology capable of producing features of almost unlimited geometrical complexity. A unique combination of the capacity to process conductive materials, design freedom, and micro- to nanoscale resolution offered by these electrochemical techniques promises tremendous opportunities for a multitude of future applications spanning microelectronics, sensing, robotics, and energy storage. This review aims to equip readers with the basic principles of electrochemical 3D printing at the small length scale. By describing the basic principles of electrochemical additive manufacturing technology and using the recent advances in the field, this beginner's guide illustrates how controlling the fundamental phenomena that underpin the print process can be used to vary dimensions, morphology, and microstructure of printed structures.

INTRODUCTION

Benefits of 3D Printing at a Small Scale

Additive manufacturing (AM), or three-dimensional (3D) printing, is a family of technologies that take advantage of material assembly, mostly (with some exceptions) (1) in a layer-by-layer fashion (2). Thanks to computer-aided design tools, it can help transform ideas and concepts into real-world objects. 3D printing is capable of producing complex features, often in a single step, thus avoiding assembly of individual parts. This offers unprecedented opportunities for flexibility in shapes and materials, providing a high degree of customization for accelerated innovation, decentralized production, and increased sustainability due to reduced overall waste. AM suits a range of length scales, from meter-sized large objects like buildings (3) or aircraft jet engine parts (4), to conventionally sized plastics printed for do-it-yourself and hobby applications and, finally, to sizes confined within micro- and nanometer dimensions. In the latter case, AM is particularly advantageous: While traditional microfabrication remains essentially within the realm of planar thin film technology, the third (vertical) dimension unlocked by AM offers almost unlimited possibilities in microsystems architecture. This drives the increasing interest in micro- and nanoscale 3D printing.

Why Electrochemistry?

Perhaps the most advanced AM technology that combines nanoscale resolution with complex designs is multiphoton stereolithography. This technique takes advantage of nonlinear light absorption that confines photochemical processes to the nanoscale (5–7). **Figure 1*a–g*** illustrates several examples of the complexity, intricacy, and level of detail that can be achieved, with structures ranging from a DNA-like interconnected double-helix (8) to toroids (9), chiral mechanical structures (10), and even microscale replicas of famous real-world objects like the London Bridge (11). This excellence, however, comes at a cost: Optical AM is generally limited to photocurable materials, mostly resins, which leave the user with their rather narrow range of electrical, mechanical, and optical properties (12). This represents a major challenge, because most modern applications require the possibility to manipulate electrical signals (in the form of voltage or current), thus demanding the processing of materials with a wide range of conductivities, which is not trivial to achieve with optical AM.

In contrast, for electrochemical methods, processing conductors or semiconductors is quite natural, and a plethora of materials can be processed, such as metals and metal oxides (13), conductive polymers (14, 15), and (conductive) biomolecules (16–18), and in a variety of material forms, including thin films (19), single crystals (20), nanoparticles (21), and composites (22, 23). Despite this obvious advantage, until recently, electrochemical techniques were not seriously considered for microfabrication, not because of fundamental limitations of electrochemical processes, but mainly because the production of the print nozzles—nanoelectrodes and nanopipettes—used to be laborious, expensive, and not always reproducible. As the nozzles become more readily available, easy to manufacture, and inexpensive, electrochemical AM (e-AM) is experiencing a boost and shows tremendous progress.

Figure 1*b–q* illustrates the capacity of e-AM to print complex features, from pillars to free-standing letters (24), coils (25), walls, arches (26), and even miniaturized art replicas (27). All of these are printed with micro- and nanoscale resolution and produced as metallic conductive structures. These advances in e-AM along with examples of current state-of-the-art and future applications are well summarized in several recent (28, 29) [and some less contemporary but also detailed (30, 31)] reviews. Therefore, instead of providing a bibliographic overview of the field, our intention here is to equip readers with the fundamentals of the micro- and nanoscale
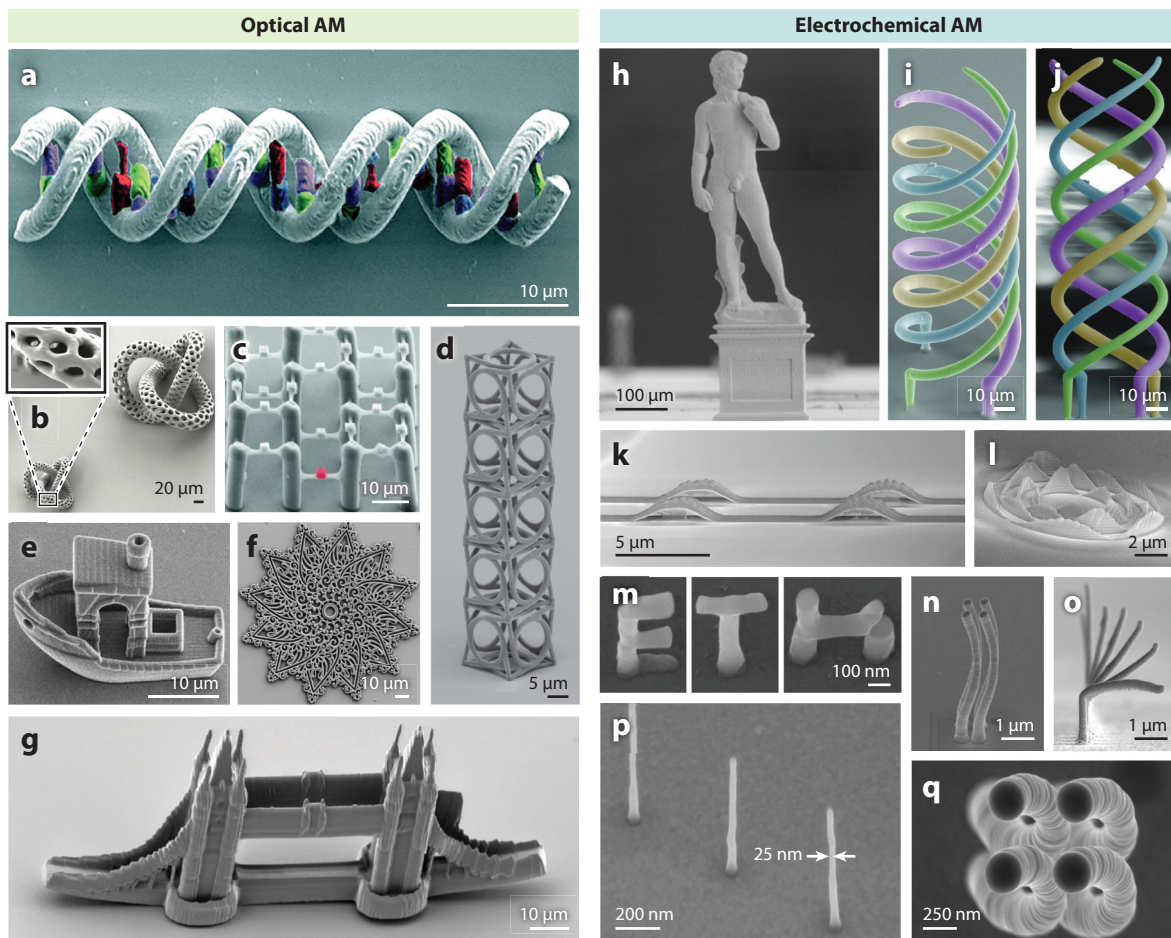
Figure 1

The capacity of optical and electrochemical AM for microfabrication revealed via grayscale and false-colored electron micrographs of various 3D structures. (*a*) DNA-like structure featuring five distinct material components (*false colored*) that connect the double helix. Panel *a* adapted with permission from Reference 8; copyright 2019 Royal Society of Chemistry. (*b*) Perforated torus knot. Panel *b* adapted with permission from Reference 9 (CC BY-NC-ND 4.0). (*c*) Two-component polymer scaffold for protein binding and cell adhesion, with a second photoresist highlighted in red. Panel *c* adapted from Reference 95 (CC BY 4.0). (*d*) 3D chiral metamaterial microstructures designed to twist in response to deformation (10). Panel *d* adapted with permission from Reference 10; copyright 2021 Springer Nature. (*e*) 3Dbenchy boat. Panel *e* adapted with permission from Reference 96 (CC BY-NC 3.0). (*f*) An acrylic mandala pattern with a diameter of 140 µm and individual features smaller than 500 nm. Panel *f* adapted from Reference 97 (CC BY 4.0). (*g*) Microscale replica of London Bridge. Panel *g* adapted from Reference 11 (CC BY 4.0). (*h*) Microscale replica (1:10,000) of David (sculpted by Michelangelo) printed with FluidFM. Panel *h* adapted from Reference 27 (CC BY 4.0). (*i,j*) Intertwined copper helices with different diameters (5, 6, 7, and 8 µm) electrochemically deposited using FluidFM (*false colored*). Panels *i,j* adapted with permission from Reference 25; copyright 2020 Wiley-VCH. (*k*) Ag arches fabricated by multimetal EHD-RP. The overhanging parts result from selective wet etching of a supporting sacrificial Cu layer. (*l*) Layer-by-layer printed out-of-plane sine waves (EHD-RP). Panels *k,l* adapted from Reference 26 (CC BY 4.0). (*m*) The letters E, T, and H printed by MCED. (*n,q*) Two different perspectives on four parallel microcoils manufactured by MCED. Panels *m,n,q* adapted with permission from Reference 24 (CC BY-NC-ND 4.0). (*o*) Straight, tilted, and overhanging pillar features by EHD-RP. Panel *o* adapted from Reference 26 (CC BY 4.0). (*p*) Copper pillars with 25-nm diameters printed with a 2-nm-aperture nozzle. Panel *p* adapted with permission from Reference 24 (CC BY-NC-ND 4.0). Abbreviations: 3D, three-dimensional; AM, additive manufacturing; EHD-RP, electrohydrodynamic redox printing; FluidDM, fluidic force microscopy; MCED, meniscus-confined electrodeposition.

electrochemical 3D printing technology. These include important considerations and underpinning phenomena, mass transport and material delivery principles, important aspects of instrumentation, and insights into printed materials in terms of chemical composition, microstructure, and corresponding mechanical properties.

FUNDAMENTALS OF ELECTROCHEMICAL 3D PRINTING

### Basic Principles and Terminology of Additive Manufacturing

Fundamentally, e-AM at the micro- and nanoscale is not different from 3D printing at any dimension. The main idea is to convert a digital model into a real-world object by using discretization. The model is sliced into layers of usually similar height, consisting of individual volumetric elements called voxels (an analogy to two-dimensional pixels, a term likely familiar to most readers), as illustrated in **Figure 2a**. The voxels are either filled with the desired material, or void, representing the empty space, where no material is placed. Smaller voxels enable smoother features and finer details to be incorporated into the structures but require more elements, following an exponential law: Reducing the voxel size by a factor of 10 results in a model containing 1,000 times more voxels. Although in digital space such discretization is effortless, in the real world, it requires longer print times. The manufacturing process becomes limited by factors such as minimal feature size, dimensions of the smallest voxel that a certain technique can produce, and resolution, the precision at which the printer can place a voxel into a given position in space. The former defines the voxels themselves, while the latter determines how well the object is then assembled. Often, lateral, or XY, resolution is differentiated from Z resolution or layer height. For electrochemical micro- and nanoscale 3D printing techniques, the terms resolution and voxel size are typically interchangeable, because in most cases nozzle positioning is orders of magnitude finer than voxel dimensions.

Electrochemical Additive Manufacturing Techniques

The primary advantage of electrochemistry for 3D printing is the possibility to convert liquid inks into solid materials via electrodeposition. The process fundamentally is rather simple, can be used for the AM of a range of materials, and offers a high degree of control of morphology and rate. It requires an electrochemical cell consisting of two or three electrodes and an electrolyte solution containing precursor species, e.g., metal ions, as well as a supporting electrolyte (inert salt to carry current) with sufficient conductivity. As the voltage needed to drive an electron transfer from the electrode surface to the precursor in solution is applied, the species are reduced into a solid. To adapt electrodeposition to AM, one should ensure that plating occurs only locally, at specified locations, and can be adapted to a layer-by-layer process. This is typically achieved via confinement, i.e., a localized delivery of precursor ions from a nozzle.

One way of localizing electrodeposition is the manipulation of fluid flow (**Figure 2b**). Fluidic force microscopy (FluidFM) (32–34) is an exemplary technology of this approach, where a microchanneled cantilever is connected to a microfluidic system to drive small amounts of precursor ink through a submicroscale or nanoscale opening at the pyramidal tip. To print a voxel, the cantilever is positioned a few hundreds of nanometers above the substrate, and the liquid ink jet hits the working electrode surface, where electrodeposition occurs.

A similar, yet different type of e-AM in a liquid environment is based on scanning ion conductance microscopy (SICM) (35), a nanoelectrochemical imaging technique illustrated in **Figure 2c**. In this case, the nozzle is a pulled glass capillary with opening dimensions ranging from several nanometers to microns, which operates by measuring the distance-dependent resistance in the gap between the tip and the substrate. The delivery principle differs slightly from FluidFM: Instead

(*Caption appears on following page*)
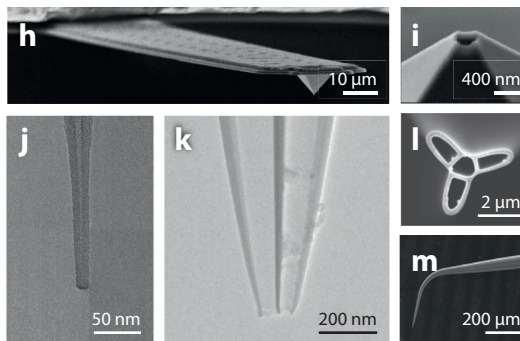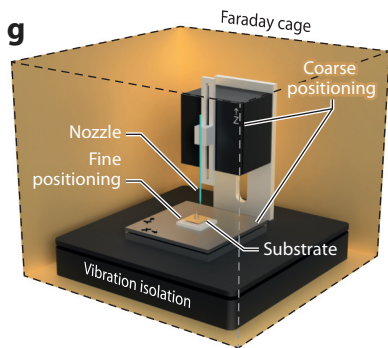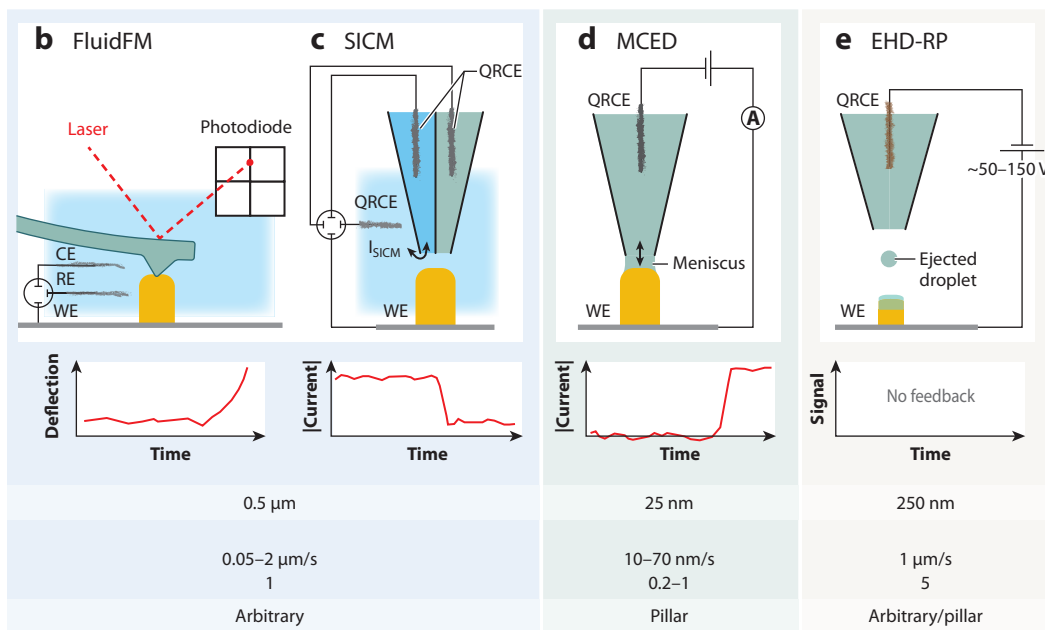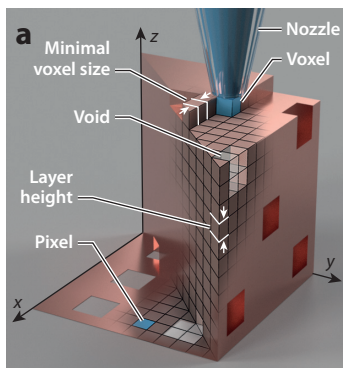
Figure 2 (*Figure appears on preceding page*)

(*a*) Schematic illustration of the 3D printing process. A copper die is fabricated by a nozzle that converts a grid of pixels in 2D and voxels in 3D digital space into a solid material structure. (*b–e*) Sketches depicting the operation of e-AM methods. (*b*) FluidFM printing in an electrochemical cell consisting of a CE and RE on a substrate that serves as the WE. A FluidFM cantilever is filled with an electrolyte and connected to microfluidic system to deliver a small volume of ink that is then electrodeposited into a solid structure. FluidFM feedback is realized by laser beam deflection on the top side of the cantilever measured with a photodiode. (*c*) A print process with SICM using a double-barrel nanopipette nozzle. Each barrel comprises a QRCE to deliver precursor ions (right barrel) or to measure a distance-dependent ion flux (I_{SICM}) in precursor-free electrolyte (left barrel). (*d*) MCED printing, based on electrodeposition in a liquid meniscus formed between the tip of a nozzle and the substrate. A two-electrode cell comprises QRCEs placed inside of the pipette, and the WE is limited by the droplet footprint on the substrate. In MCED, the feedback detects faradaic current measured when the meniscus is formed. (*e*) EHD-RP printing. As high voltage is applied to the sacrificial metal wire inside the nozzle, a small droplet containing generated metal ions is ejected onto the substrate (WE), where the content is converted into a solid via electrodeposition. (*f*) Key performance characteristics of e-AM methods. (*g*) Schematic of the general instrumentation for e-AM. The setup is built on top of a vibration isolation platform to diminish mechanical disturbances. A combination of coarse (motors) and fine (piezo elements) positioning systems allows for a wide range of operation while maintaining high resolution and dynamic performance. The positioning systems move either the nozzle or substrate. Faraday cages (and optionally also an acoustic enclosure) are used to reduce electromagnetic (and acoustic) perturbations. (*h–m*) Electron microscopy images of the different nozzle types, including (*h*) a FluidFM cantilever with a closeup of the pyramidal tip (*i*), (*j*) a quartz nanopipette nozzle with a 2-nm opening, and (*k*) a double-barrel pipette with orifice diameters of ~50 nm. Panels *h,i* adapted with permission from Reference 43, copyright 2014 Elsevier; panel *j* adapted with permission from Reference 24 (CC BY-NC-ND 4.0); panel *k* adapted with permission from Reference 36, copyright 2016 American Chemical Society. (*l*) A three-barrel glass pipette orifice. Panel *l* adapted with permission from Reference 45; copyright 2018 American Chemical Society. (*m*) A single-barrel glass pipette tip bent with a microforge. Panel *m* adapted with permission from Reference 47; copyright 2018 Wiley-VCH. Abbreviations: 2D, two-dimensional; 3D, three-dimensional; CE, counter electrode; e-AM, electrical additive manufacturing; EHD-RP, electrohydrodynamic redox printing; FluidFM, fluidic force microscopy; MCED, meniscus-confined electrodeposition; QRCE, quasi-reference counter electrode; RE, reference electrode; SICM, scanning ion conductance microscopy; WE, working electrode.

of liquid flow, the precursor ions are supplied by electromigration, induced by the applied voltage across the nozzle using a quasi-reference counter electrode (QRCE) (36, 37).

Meniscus-confined electrodeposition (MCED) (38–40) uses a drastically different principle to confine printing to a small area. In this case, electrodeposition is localized in a liquid meniscus, a droplet that forms between a nanopipette nozzle and a conductive substrate (**Figure 2d**). The print nozzle is not immersed into liquid, and only a minute electrolyte droplet (somewhat close in diameter to the nozzle opening) limits the area where deposition can occur on the substrate. Printing starts immediately as the meniscus is formed and, as long as the cathodic voltage is applied, requires a retraction of the nozzle to avoid clogging.

Unlike meniscus-confined techniques where the droplet forms a continuum with the rest of the electrolyte solution in the nanopipette, in electrohydrodynamic redox printing [EHD-RP (26)] individual droplets are ejected from the nozzle positioned several microns away from the conductive surface (**Figure 2e**). Droplets, typically in dimensions somewhat smaller than the nozzle opening size, are formed due to high (ca. 50–150 V) constant voltage applied to the wire inside the nozzle. The large electric field on the order of $\sim 10^7$ V m^{-1} helps to overcome the ink surface tension, while the sacrificial electrode wire oxidation supplies metal ions to the nozzle tip. Electrodeposition occurs when the ejected liquid lands on the conductive substrate and electron transfer converts the droplet content (ions) into a solid metal.

The particularities of each technique provide a range of advantages or disadvantages in terms of resolution, print rates, and voxel shapes and arrangement (**Figure 2f**). For example, printing in liquid environments with FluidFM or SICM is typically rather limited in resolution, allowing minimum feature sizes around 0.5 micrometers (25, 27, 36). EHD-RP is capable of about half of that for out-of-plane features (26), whereas MCED reaches a 25-nm resolution mark (24). Print rates are also substantially different because of the drastically different delivery mechanism, with FluidFM, SICM, and MCED approaching approximately 1 voxel s^{-1} and EHD-RP being fivefold

faster. The performance in 3D printing, however, is also largely influenced by qualitative factors, such as the complexity of printed features and continuity of structures, which depend on voxel shapes and how the voxels are placed with respect to each other. In this regard, there is also a large distribution across e-AM methods, with in-liquid techniques such as FluidFM able to produce very complex features, with or without support structures, given by the possibility to place voxels in almost any arrangement (**Figure 1*b–j***). On the other end of the spectrum is meniscus-based printing, where voxels are typically straight pillars (**Figure 1*p***), which are more difficult to place in tighter structures to create other than column-like objects; some exceptions of more complex structures are shown in **Figure 1*m*, *n*, and *q***. EHD-RP is somewhat in the middle between these two extremes, meaning that various structures can be produced, but so far the intricacy is limited to pillars or walls (**Figure 1*l,o***), as the arches in **Figure 1*k*** are produced by etching a sacrificial (also 3D printed) layer.

Instrumentation

Being a relatively new discipline in the field of 3D printing, e-AM systems remain mostly custom-made with few commercial products available. Among those exclusively tailored to printing, a FluidFM-based system has been commercialized. Commercial instrumentation offers advantages, as it provides a ready-to-go solution, but because the field is still in development, custom-made platforms often seem more versatile by offering flexibility in experimentation for expanding available techniques and materials.

General considerations. Depending on the technique, the required equipment varies slightly, but the common principles remain the same. A typical e-AM system (**Figure 2*g***) consists of a nozzle and material delivery apparatus, a positioning system, isolation to protect from electromagnetic, mechanical, and acoustic noise, and (ideally) a feedback mechanism for nozzle positioning/voxel detection. Delivery of the material and the printing mechanism are probably the most fundamental aspects, but the current aspiration of bringing AM to the nanoscale requires attention to each of these details. Even the most trivial of them, e.g., isolation from external disturbances, requires (*a*) damping of mechanical vibrations (which is particularly difficult at the lower end of the frequency spectrum) with active and passive isolators, including heavy table supports and vibration isolation platforms; (*b*) acoustic enclosures with acoustic foam to reduce nozzle/sample vibrations and improve electrical recordings (41); and (*c*) Faraday cages for electromagnetic noise reduction. These cages can be particularly important when measuring small currents (nanoamperes, picoamperes, and below) in MCED or SICM, requiring the use of specialty isolated cables (typical banana wires are to be avoided when possible) and careful grounding of all equipment and cables using dedicated ground lines. Notable, however, is that measurements of small currents with high recording rates as needed in e-AM are difficult and have fundamental limitations (42).

Nozzles. Microchanneled cantilevers for FluidFM (**Figure 2*b***) are produced using cleanroom-based microfabrication procedures, including several patterning, deposition, and etching steps (43). A particular advantage of microfabricated nozzles is the possibility to vary nozzle geometry and size in a rather broad range, from tipless cantilevers to small, 5-nm-aperture nanopores (44) for single-molecule sensing. However, among the different tip geometries, a pyramidal tip (**Figure 2*i***) is mostly used for e-AM, with diameters ranging from 100 nm to several micrometers (25, 27).

Glass micro- and nanopipettes employed in MCED and EHD-RP, in contrast to FluidFM probes, do not require cleanroom facilities. Commercially available pipette pullers serve as a versatile tool for the rapid fabrication of print nozzles of various sizes from a range of capillary and glass types. In a pulling process, a preprogrammed sequence is designed to heat up the center of

a glass capillary with a laser or filament, while mechanical pulling forces applied on the capillary ends separate the softened glass, thus creating two fine tips. Material selection is important: Nozzles with diameters of 100 nm and larger are fabricated from softer borosilicate glass, whereas nanoscale dimensions require quartz with significantly higher melting temperatures. For applications in MCED, single-barrel nozzles as small as 1 nm in diameter are reported (24) (**Figure 2j**). Multibarrel nozzles with two compartments (**Figure 2k**), as used in SICM printing (36) or multi-material EHD-RP (26), and three (45) or even four (46) compartments (the latter is not employed for printing) can also be fabricated in a similar way (**Figure 2l**). Using a microforge, the straight pipettes can be bent (47) into cantilever-like nozzles (**Figure 2m**).

Positioning. When choosing the appropriate positioning system, precision, speed, stability, and repeatability of nozzle placement are the key factors to consider. At the microscale, positioning is possible with stepper motors, which often offer nanoscale precision according to their technical specifications. However, as voxel dimensions approach the submicroscale or nanoscale, motors often fail to fulfill most of the above key factors. For higher precision, the choice turns to piezo-electric actuators, which offer subnanometer precision and high translation speed with millisecond or even submicrosecond positioning time but are limited by small travel ranges. Typically, the dynamic performance is inversely proportional to the motion range. For commercial systems the resonant frequency can be about 10 kHz for a range of a few microns, but as the range increases to tens of microns, this metric drops down to 1 kHz and further to a few hundred Hz at scales approaching 100 µm. One should also remember that the repeatability of piezo systems is usually limited by 1% of the travel range, which is a crucial factor to consider for layer-by-layer printing, as nozzles should repeatedly scan over the same areas multiple times. The problem of covering large travel ranges can be overcome by combining fine piezopositioners with high dynamic performance with coarser motor movement. While this clearly solves the issues for printing on larger areas, attention must be paid to the mechanical stability of such a combined system. Other instrumental solutions are also possible when using less conventional approaches: A recently proposed open-source nanopositioning system is based on a magnet driving system in combination with an inexpensive piezo stack element (48).

Drift of piezo elements presents another important consideration, which can be stabilized by tight temperature control. Moreover, in a layer-by-layer printing process, displacement hysteresis, creep, and other nonlinearities in piezo positioning play an important role (49, 50). In commercially available systems, closed-loop control or internal circuitry usually solves these issues but at the expense of dynamic performance.

Feedback. Contrary to meso- and macroscale 3D printing, where voxel growth detection is mostly unnecessary, at a small scale, and especially with e-AM, it is often compulsory to control the printing process. Surveillance of the voxel growth with microscopy methods is a good addition, but this lacks spatial resolution and therefore is unsuitable to completely fulfill this task. Therefore, e-AM methods often rely on feedback mechanisms for process automation.

The intrinsic strength of FluidFM is its atomic force microscopy (AFM) capacity that helps to track voxel growth via sensing laser beam deflection (33). The reflective top surface of the FluidFM cantilever reflects a laser beam, which is further detected with a photodiode. As the growing structure under the cantilever's aperture touches the cantilever, the deflection of the laser changes, resulting in a different voltage value measured at the photodiode (**Figure 2b**), thus informing about the completion of a voxel. The challenge is to prevent the nozzle from clogging because the cantilever deflection occurs only upon direct mechanical contact between the growing voxel and the cantilever tip, making feature-cantilever contact unavoidable. Another potential issue is related to gas bubbles evolving when printing metals that require large cathodic voltages. In this

case, the bubbles can prematurely trigger the feedback by interrupting the laser beam propagation in the electrolyte.

One way to overcome these issues is to employ a non-optical contactless feedback, originating from the detection of ionic current in SICM. In that case, the electrical resistance of the tip-substrate gap informs about the voxel state: When this distance decreases, the ion flow becomes hindered, causing changes in either the DC or AC impedance (36, 37, 51) (**Figure 2c**). Usually, the feedback is sensitive enough to detect gap distances in the order of the orifice radius (52). In a double-barrel nozzle configuration one of the compartments is employed for local ion delivery and the other one for the feedback signal. A control system can be used to keep the tip-substrate distance constant, allowing constant retraction of the nozzle with the growing voxel. Despite the intrinsic simplicity, the feedback to maintain constant distance between the printed features and the nozzle can become complicated due to local conductivity changes under the tip caused by the electrodeposition process. Thus, disadvantages of an SICM feedback are related to its sensitivity to the local environment, but also to the more complicated electrical arrangement and its susceptibility to electromagnetic noise and bubbles.

MCED also sometimes relies on a non-contact feedback, but as the method is executed in air the current is measured only when a meniscus is present (**Figure 2d**). Therefore, as soon as the meniscus is established and the overpotential is high enough, the deposition starts and the nozzle needs to be retracted to allow the voxel to grow. The issue with this approach is that the current can only inform about the existence of the meniscus but cannot further measure the distance between the tip and the growing voxel. One way to overcome this limitation is to incorporate a different form of feedback based on other physical phenomena. This has been successfully demonstrated with MCED printing using a tuning-fork (AFM-like) distance control (53). Another solution is to frequently interrupt the print process by repeatedly breaking the meniscus after its formation (24, 54). This way, with each landing, only a minute amount of material is deposited (with a total amount of charge down to a few femtocoulombs), and nozzle clogging is prevented even at scales down to 25 nm (24).

EHD-RP is the only e-AM method that currently lacks instrumental feedback, and positioning of the nozzle is achieved via optical microscopy alone. Although this is sufficient for nozzle-substrate distances of 10 μm, the absence of feedback during printing leads to several challenges, including autofocusing of droplet delivery [and hence the inability to reach close spacing when printing pillars (55)], variation of material structure upon decreasing the nozzle-substrate gap, and difficulties in the precise control of deposition rates when printing multiple materials (26). Attempts to track voxel growth by monitoring the deposition current were thus far unsuccessful due to the large contribution of non-faradaic (capacitive) processes to the measured signals (56). Integration of the EHD-RP with a contactless feedback mechanism will help to overcome these issues.

Material Delivery Principles

The different e-AM techniques vary in the way the precursor ions are delivered to the location where the voxel is formed. These material delivery principles include a pressure-driven flow of liquid, droplet generation in high electric fields or (electro-)chemical manipulation of ionic fluxes to supply the desired species. The underlying physical principles play a crucial role in controlling the outcome of the deposition.

Fluid flow. FluidFM operates by manipulation of very small liquid volumes, down to subpicoliters (57), but the sole flow parameter that the user can usually control is the overpressure across the nozzle. This is simply an instrumental limitation, because other quantities, such as flow rate, are

difficult to measure at these scales. The relationship between the applied overpressure and the resulting flow rate is not trivial for FluidFM owing to the complex nanopipette geometry. It requires numerical simulations, but general considerations can also be derived from the well-known relationship for pipe flow, known as the Hagen–Poiseuille law (58):

$$Q = \frac{\pi \Delta p r^4}{8 \mu L},$$ 1.

where Q, Δp, L, r, and μ denote the volumetric flow rate, the pressure difference between nozzle ends, nozzle length, nozzle opening radius, and the dynamic viscosity of the liquid, respectively. The crucial consideration for e-AM printing is related to the fact that a reduction of the nozzle diameter is accompanied by an exponential (power of 4) drop of the flow rate through the nozzle. In printing terms, this means that when attempting to improve the resolution by reducing the nozzle size by an order of magnitude, one should encounter a material delivery rate four orders of magnitude lower, thus denoting tremendously reduced print speeds (in material volume per unit time). Indeed, manipulating liquid flow through nozzles that approach the single-digit nanometer scale (as in **Figure 2j**) for improved resolution using pressure-driven flow would be not only impractical but most likely close to impossible.

A more detailed consideration of the printing process with FluidFM can become available when considering hydrodynamics in combination with the electrochemical faradaic process (27). Such a description can be inferred from a so-called wall-jet electrode configuration, where a jet of solution of electroactive species is pushed from a circular nozzle to hit the working (collector) electrode perpendicularly. The electrode current I and thus the rate of electrodeposition can be approximated by the analytical expressions that relate geometry (nozzle r and collector electrode radius R_c), electrolyte species diffusivity D, and the parameters of the fluid flow (59):

$$I = 1.6 k z F c_0 D^{2/3} v^{-5/12} r^{-1/2} R_c^{3/4} Q^{3/4},$$ 2.

where k, z, F, v, and c_0 specify geometric proportionality factor, number of electrons in the elementary electrochemical reaction, Faraday constant, kinematic viscosity, and concentration of precursor ions, respectively.

This relationship only qualitatively describes a particular case of FluidFM. The tip geometry and the applied pressure influence the area where the precursor ions are collected to transform into a solid. Nevertheless, Equation 2 was shown to predict reasonably well the voxel diameters as well as vertical and volumetric print rates for a wide range of pressures (10–200 mbar), as shown in **Figure 3a** and **b**, respectively (27). As shown, the amount of printed material increases almost linearly with overpressure ($\propto \Delta p^{3/4}$). However, the effect of voltage on feature growth is also very noticeable (**Figure 3a**), allowing one to fine-tune the e-AM process. Higher cathodic potential (**Figure 3c**) leads to more efficient precursor collection at the substrate, meaning finer voxels with a smoother surface finish. Thus, the resolution can vary by a factor of almost two (at 200 mbar) by switching between −0.42 V and −0.50 V. This allows feature sizes to be adjusted on the fly (25, 27), even with a single nozzle, as shown in **Figure 1i,j**, where each coil has a different diameter.

Diffusion and electromigration. Mass transport effects also play a key role in the performance of MCED. When ignoring additional contributions from other electromigration and convection due to solvent evaporation at the meniscus, the rate of electrodeposition is limited by the diffusion-controlled current, I. Its value corresponds to the amount of the printed material and thus can be used as a benchmark to estimate the print rate. Considering that the pipette with semiangle α restricts the mass transport by the solid angle Ω, one obtains (60):

$$I = \Omega z F D c_0 \frac{r}{\sin[\alpha]} = 2\pi (1 - \cos \alpha) z F D c_0 \frac{r}{\sin[\alpha]}.$$ 3.

As can be seen, the current magnitude is directly proportional to the pipette radius, which means that as the voxel dimensions scale with r^3, printing at higher resolution with smaller nozzles results in significantly faster deposition in terms of voxels per unit time: 10-nm voxels are printed two orders of magnitude faster than voxels with diameters of 100 nm. That has important consequences for MCED: (*a*) Efficiency at larger dimensions (scales of millimeters and above) is typically low due to limited mass transport, and (*b*) print rates at the nanoscale are becoming
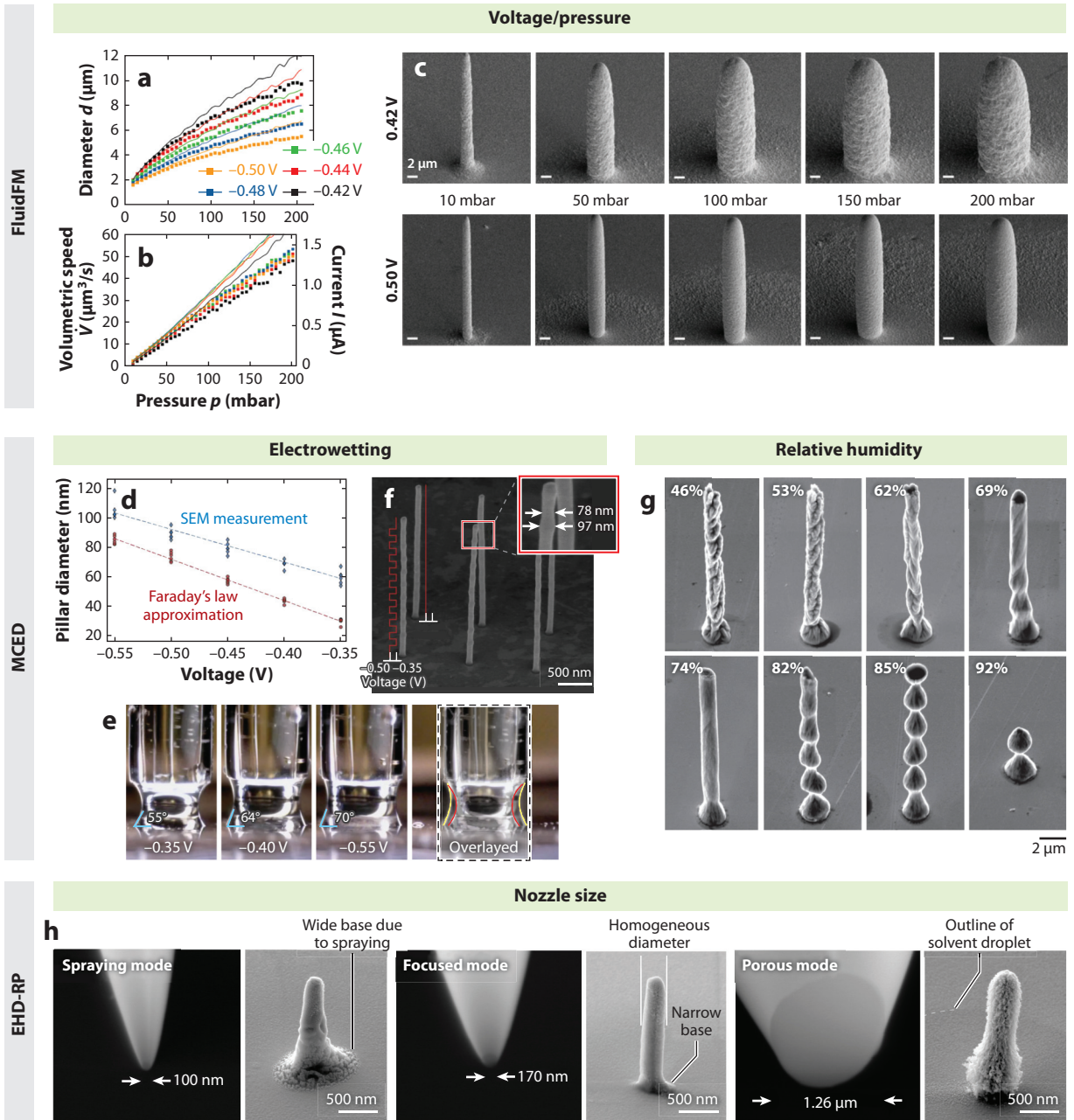
(*Caption appears on following page*)

Figure 3 (*Figure appears on preceding page*)

Key factors of consideration in micro- and nanoscale e-AM. (*a*) Pillar diameters and (*b*) volumetric print rate dependence on the applied pressure at different substrate voltages in FluidFM (experimental data and fitted model values are shown with *dashed* and *solid lines*, respectively). (*c*) A series of SEM images of pillars printed with FluidFM (300-nm opening) at voltages of −0.42 V and −0.50 V and applied pressures ranging from 10 to 200 mbar. Panels *a–c* adapted with permission from Reference 27 (CC BY 4.0). (*d*) Effect of deposition voltage on pillar diameters in MCED, as measured using SEM (*blue diamonds*) and calculated (*red circles*) from the current data using Faraday's law of electrolysis. (*e*) Images of menisci formed at the end of an unpulled capillary (1-mm outer diameter) at voltages of −0.35, −0.40, and −0.55 V. Overlayed image of the meniscus formed at −0.35 V (*transparent*, *grayscale*) on top of the image of the meniscus at −0.55 V (*colored*). The two menisci are marked by the dashed lines in red and yellow for −0.35 V and −0.55 V, respectively. (*f*) SEM image of MCED-printed pillars with (*front row*) and without (*back row*) diameter modulation for a nozzle size of 50 nm. Print voltage is varied between −0.35 V and −0.5 V (*squared red line*, *front row pillars*) or kept constant (*straight red line*, *rear row pillars*). Panels *d–f* adapted with permission from Reference 24 (CC BY-NC-ND 4.0). (*g*) SEM images of Co/Cu alloy pillars printed with MCED at different relative humidities. Panel *g* adapted with permission from Reference 63 (CC BY-NC-ND 4.0). (*h*) Nozzle effect on printing with EHD-RP. The corresponding nozzle images and printed structures are shown in sequence from left to right. Panel *h* adapted from Reference 26 (CC BY 4.0). Abbreviations: e-AM, electrical additive manufacturing; EHD-RP, electrohydrodynamic redox printing; FluidFM, fluidic force microscopy; MCED, meniscus-confined electrodeposition; SEM, scanning electron microscopy.

fast, thus requiring a high-speed feedback mechanism and dynamic positioning system to achieve appropriate nozzle movement to avoid nozzle clogging.

Electrowetting. MCED offers a possibility to tune voxel sizes on the fly by changing the applied voltage (24), as shown in **Figure 3***d*. This seems to be related to electrowetting, which is a change in the wettability of an electrode surface due to an applied potential difference, as described by the Young–Lippmann equation (61):

$$\cos[\theta] - \cos[\theta_{eq}] = \gamma_{LA}^{-1} \int_{V_{pzc}}^{V} C(V)\,V\mathrm{d}V, \qquad 4.$$

where θ, θ_{eq}, denote the droplet contact angle under applied voltage V and at equilibrium ($V = V_{pzc}$), whereas γ_{LA}, V_{pzc}, and $C(V)$ specify the surface tension of the liquid/air interface, potential of zero charge of the electrode, and voltage-dependent capacitance, respectively. This relation attributes the change of contact angle of the liquid droplet θ (with respect to its equilibrium value θ_{eq} at the potential of zero charge V_{pzc}) to the voltage-dependent capacitance of electrolyte $C(V)$ and the applied voltage V. With typical capacitance values from several to tens of μF cm^{-2}, one can anticipate a significant change in wettability, featuring tens of degrees of change upon application of hundreds of millivolts of a potential difference. Exactly that behavior is observed experimentally at a micro- and millimeter scale (**Figure 3***e*), but there are certainly more complications that contribute to wetting behavior, namely (*a*) adsorption phenomena observed for different electrolyte ions, (*b*) concentration effects and, probably most importantly, (*c*) the influence of faradaic processes on electrowetting (61). In addition, a nonclassical geometry (micro- or nanopipette meniscus with an almost infinite reservoir of liquid versus droplet with a finite volume), electrodeposition of a dissimilar material to a substrate itself, and a change of geometrical arrangement (growing voxel) introduce further complications to the effect of electrowetting in 3D printing. By controlling electrowetting, however, it becomes possible to adjust nanoscale voxels for nanostructures with variable AM resolution (**Figure 3***f*).

Evaporation. For meniscus-based printing, the considerations for mass transport, ion flow, and meniscus stability play an important role, especially in the absence of active feedback. **Figure 3***g* illustrates how relative humidity (RH) influences the evaporation rate and thus has an enormous effect on the deposition results (62–64). The surface of the printed structures is rather rough at lower humidity levels. Optimal smoothness is reached at an RH of 74%. At RH levels >82%,

synchronization of growth rate and nozzle withdrawal become unbalanced, leading to uneven deposition and eventually fully impaired printing at 92% RH. Precise theoretical treatment of evaporation in a meniscus seems to be a complicated task. Even though the evaporation rate can be classically inferred using the Hertz–Knudsen relation [which, however, is not always quantitative (65)], numerical simulations are required to account for evaporation in a rather complex mass transport inside the meniscus (66, 67). Calculations have shown that evaporation even at an RH of 70% can reach rates approaching 4,000 meniscus volumes per second (67), with lower humidity levels responsible for a higher concentration of metal ions in the meniscus and thus higher print rates. However, care must be taken when printing at very low humidity levels because electrolyte salts start to crystallize and block the nozzle. In addition, one has to consider that, in nanoscale environments, evaporation rates are also strongly dependent on other factors (surface hydrophobicity and nozzle opening) (68).

Factors to consider in EHD-RP. In EHD-RP the electric field pushes electrolyte ions toward the nozzle end, helping to overcome surface tension and eject liquid toward a substrate. Generally, this occurs in two regimes: jetting and dripping. For both regimes, scaling laws are rather difficult to derive, and so-called stability windows of each mode are determined empirically. However, several general concepts exist. First, the voltage required to break the surface tension is proportional to its square root $V \propto \gamma^{1/2}$, meaning that liquids with smaller γ require lower voltage (69). Second, the size of the jet r_j and, hence the resolution, scales according to

$$r_j \propto \frac{1}{E}\sqrt{\gamma r}, \qquad\qquad 5.$$

where E is the electric field between the nozzle and the substrate (70). Following Equation 5, the increase in E results in a smaller jetting diameter. These laws, however, are only a guideline. In EHD-RP, printing occurs not in a jetting mode but in a dripping mode, and the frequency of droplet generation is crucial. At higher voltages the frequency increases, allowing for a higher droplet rate. This, however, can also be problematic, as liquid must evaporate rapidly enough to avoid accumulation on the substrate. The nozzle size plays an important role in the balance of electrostatic and capillary forces. Experimentally, EHD-RP has been shown to operate most efficiently using nozzles with 170 nm apertures, which help to fabricate stable and homogeneous features (**Figure 3***b*). Larger or smaller nozzles lead to significantly less-consistent structure shapes (26).

There are also several other important phenomena in AM with EHD. First, the user must remember that printing from electrolytes containing salt solutions is difficult, as only the excess of ions in each droplet is converted into the metal (56, 71). Therefore, sacrificial metal anodes are typically preferred as the ion source in EHD (26). Second, there is a strong autofocusing effect in EHD, meaning that the electric field directs the landing droplets precisely on top of the previously printed features (55). On one hand, it is beneficial because it allows remarkably consistent delivery of droplets toward the printed pillar structures. On the other hand, it can be detrimental for printing closely positioned features, which so far has prevented EHD-RP from printing pillars with spacing <500 nm (and walls with spacing <250 nm) (26).

PROPERTIES OF THE PRINTED MATERIALS

Morphology

Each technique has its own unique effect on the morphology of the printed features. **Figure 4***a* reveals the differences in the shape and surface finish of Cu pillar structures fabricated by FluidFM, MCED, and EHD-RP (72). Pillars printed in liquid (FluidFM) appear significantly rougher than those fabricated by in-air techniques (MCED and EHD-RP).
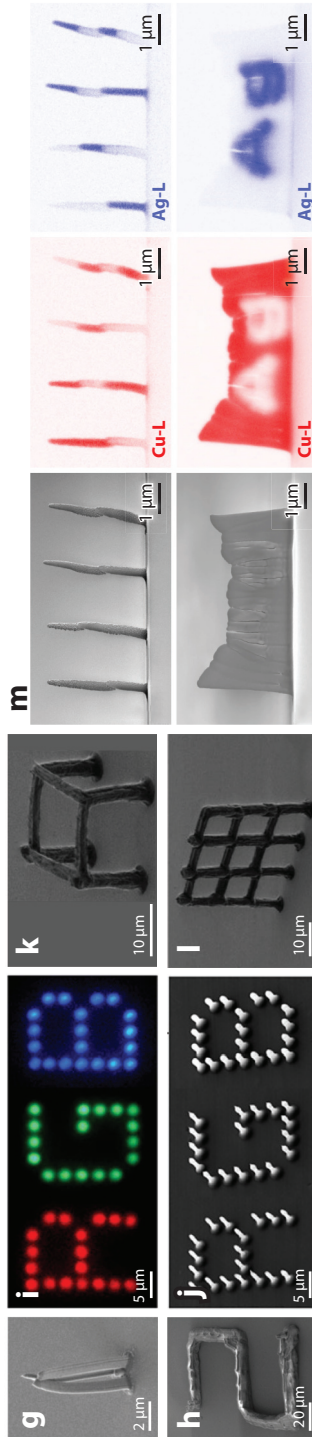
Morphology
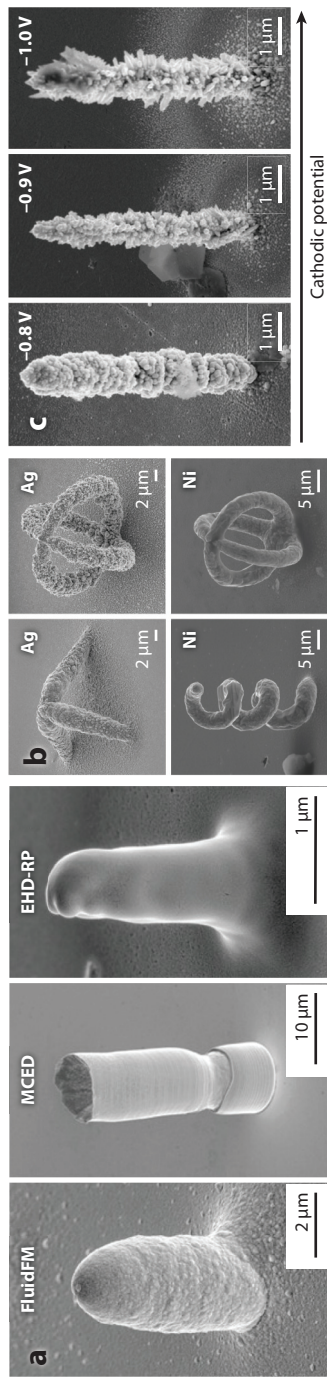
Microstructure
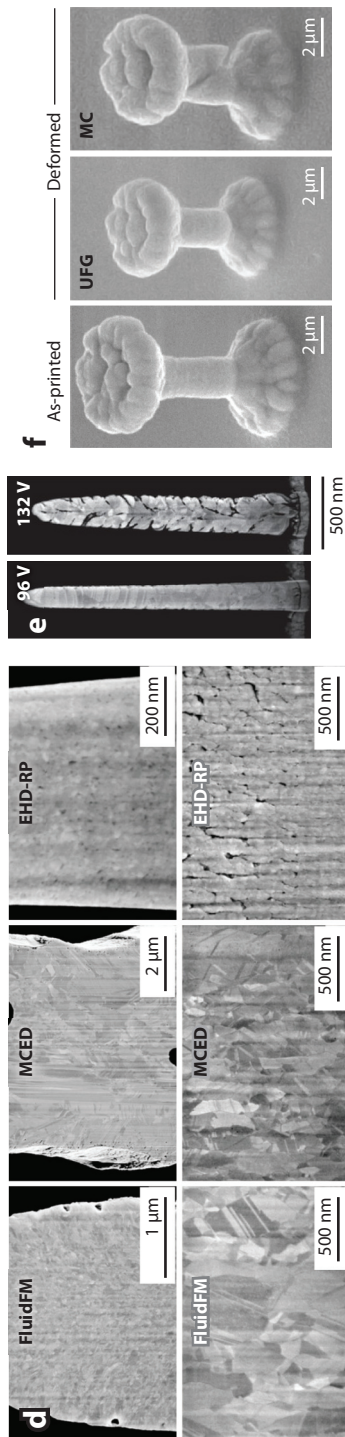
Materials library

(Caption appears on following page)

Figure 4 (*Figure appears on preceding page*)

Morphology and microstructures of different materials and electrochemical printing approaches. (*a*) Copper pillars fabricated by FluidFM, MCED, and EHD-RP. Panel *a* adapted with permission from Reference 72; copyright 2020 Wiley-VCH. (*b*) Tripod, double-ring, and helical structures fabricated in Ag and Ni with FluidFM. (*c*) Ag pillars printed with FluidFM at different voltages with the same overpressure of 10 mbar. Panels *b,c* adapted with permission from Reference 73 (CC BY-NC-ND 4.0). (*d*) Cu pillar (*top row*) and pad (*bottom row*) cross sections fabricated using FluidFM, MCED, and EHD-RP exposed by focused ion beam. Panel *d* adapted with permission from Reference 72; copyright 2020 Wiley-VCH. (*e*) Cross sections of pillars printed with EHD-RP at voltages of 96 V and 132 V. Panel *e* adapted from Reference 74 (CC BY 4.0). (*f*) Dog-bone-shaped Cu pillars before and after compression experiments with UFG and MC microstructure. Panel *e* adapted from Reference 77 (CC BY 4.0). (*g*) Electron micrograph of three polymer (PEDOT:PSS/polypyrrole composite) wires printed with a multi-barrel nozzle. Panel *g* adapted with permission from Reference 45; copyright 2018 American Chemical Society. (*h*) Metal-organic framework (HKUST-1) structure obtained by evaporation in a meniscus-guided printing. Panel *h* adapted with permission from Reference 88; copyright 2022 American Chemical Society. (*i,j*) Optical photoluminescence and electron microscope images of perovskite pillars (diameter 600 nm and height 5 μm) printed by non-e-AM. Panels *i,j* adapted with permission from Reference 98; copyright 2020 American Chemical Society. (*k,l*) 3D-printed virus microstructures fabricated by non-e-AM. Panels *k,l* adapted with permission from Reference 92 (CC BY 4.0). (*m*) SEM images and corresponding EDX elemental maps of Ag/Cu pillars (*top row*) and A- and G-shaped Ag features embedded in a Cu wall structure fabricated by multimaterial EHD-RP with a double-barrel nozzle. Panel adapted from Reference 27 (CC BY 4.0). Abbreviations: e-AM, electrical additive manufacturing; EDX, energy dispersive X-ray spectroscopy; EHD-RP, electrohydrodynamic redox printing; FluidFM, fluidic force microscopy; MC, microcrystalline; MCED, meniscus-confined electrodeposition; SEM, scanning electron microscopy; UFG, ultrafine grain.

Indeed, the morphology of the feature printed by the same technique can vary. **Figure 4*b*** shows that the choice of materials for printing with FluidFM can be crucial. Ni features evidently appear smoother than corresponding Ag counterparts (73). This difference seems to be mainly attributed to two factors: intrinsic microstructure of the material and the effect of process parameters on growth process on the surface and inner microstructure formation. In the abovementioned example, both metals exhibit small submicroscale-sized grains (50–150 nm for Ag and elongated 50–250 nm, resembling a dendrite for Ni). Ag requires a high overpotential to reach reasonable print rates, which is not the case for Ni, and the structures appear significantly rougher. This voltage effect illustrated in **Figure 4*c*** shows higher cathodic voltages leading to features with increasingly spikier surfaces (73). This is likely attributable to the nucleation and growth mechanisms, where an increased number of nucleation sites at higher cathodic voltages results in a rougher surface. Sometimes, the effect of voltage can be even more pronounced and affect the overall geometry and not only the morphology. For example, application of a nonuniform voltage profile during electrodeposition in MCED has been shown to change the structures' shapes from pillars to hollow tubes (64).

Microstructure

Fundamental differences in the deposition process across techniques also manifest themselves in the microstructure (**Figure 4*d***). Polycrystalline materials produced by more classical e-AM, such as FluidFM and MCED, reveal dense features with minimum void content, whereas EHD-RP tends to result in porous (but also polycrystalline) materials. Grain sizes typically vary from tens to hundreds of nanometers and depend on the chosen material.

Some control over the microstructure can be gained by adjusting printing conditions. For example, the voltage in EHD-RP exerts a large influence on the microstructure (grain sizes) and morphology of the deposits (**Figure 4*e***). At higher potentials, the total volume of precursor solution landing on the substrate increases to a point when the droplets do not have enough time to evaporate, leading to a constantly present solvent on the substrate. This difference in solvent coverage causes increased grain size and increased feature sizes when the solvent covers the whole feature. Grain size can then be tuned on the fly with applied voltage (74). Other techniques such

as MCED can offer even finer control. For example, pulsed deposition results in smaller, thinner, so-called nanotwinned grains that can significantly change the mechanical characteristics of the printed structures (75). Microscale 3D printed structures with nanotwinned copper exhibit a 10% higher elastic modulus (obtained by nanoindentation experiments) compared to the bulk material (128 versus 117 GPa, respectively). Induction of concentration gradients by shear flow and uneven evaporation of the meniscus can also yield nanotwinned microstructures (76) with an even higher elastic modulus (155 GPa). In the case of FluidFM, the microstructure (ultrafine versus micro-crystalline) of geometrically equivalent features is random but has similar consequences for the material's properties. A study of 3D printed dog bone–shaped pillars (77) demonstrated that features with finer grains with an average grain size of 170 nm deform uniformly upon stress, whereas the microcrystalline features (410-nm grains) exhibit shear-like deformation with significantly lower yield strength.

Material Library: Beyond Metals and Toward Multimaterial Printing

Once it comes to the selection of printable materials for e-AM, metals that can be electrodeposited are preferred. Thus far, metallic structures of Ag (26, 73), Ni (73), Pt (38, 78), and some alloys, including Co/Cu (63), Cu/Ag (26), Ni/Cu (79), Ni/Mn (80), and Ni/Co (80), have been realized with 3D micro- and nanoprinting, with Cu being the most popular material choice for e-AM. Because electrodeposition is generally not limited to only metals, e-AM offers processing of other materials, e.g., conductive polymers such as polyaniline (81). Processing of insulating (non-conductive) polymers by e-AM, however, is not feasible. This issue can be addressed by non-electrochemical meniscus-based approaches similar to MCED capable of printing both conductive and insulating structures. In this case, polymerization can be induced, e.g., by oxidation of the monomer in the meniscus by air (82). Otherwise, the growth occurs due to rapid evaporation of the solvent, allowing 3D printing of various polymers (45, 83–85) (**Figure 4g**). FluidFM is also suitable for printing polymers that form in a chemical (non-e-AM) way (86, 87). Other materials, including metal-organic frameworks (88) (**Figure 4b**), perovskites (89, 90) (**Figure 4i,j**), supramolecular structures (91), and even virus assemblies (92) (**Figure 4k,l**) were fabricated by non-e-AM meniscus guiding. EHD (in its non-electrochemical configuration) is also a powerful technique to process a plethora of various materials (93, 94).

A special advantage of e-AM compared to many non-electrochemical methods is related to the recent advances in multimaterial printing capabilities. Electrochemistry offers several mechanisms to achieve control over the chemical composition of 3D printed structures. In MCED, for example, relative humidity (63) (**Figure 3g**) or the deposition voltage (79, 80) can be used to vary the metal content of the printed features. In these cases, deposition occurs from a single electrolyte with a fixed composition. This approach has limitations in fabricating pure uncontaminated components, requiring more than one ion source. EHD-RP with double-barrel capillaries (26) and two sacrificial anodes (Cu and Ag) allows manufacturing of multimetal and alloy structures (**Figure 4m**). As the process is controlled dynamically by switching the voltage between nozzle barrels, the composition can be alternated as fast as every 100 ms. The capacity to combine multiple materials in a structure opens an entirely new dimension in additive micromanufacturing.

CONCLUSIONS AND PERSPECTIVES

e-AM is a family of emerging technologies that allow microfabrication in all three dimensions. In contrast to many other techniques, e-AM can naturally process conductive materials, primarily metals, that are generally unavailable to other micro- and nanoscale AM technologies based on nonelectrochemical principles. This unique advantage is, however, underpinned not exclusively by

electrochemical science alone. It also requires a holistic understanding of fundamental principles in areas as diverse as fluid dynamics, chemical species mass transport, speciation, surface science, crystallography, and many others, not to mention the need for advanced engineering solutions in electronics and software. Our beginner's guide attempts to give readers an overview of the most important factors to consider for 3D printing at small scales with e-AM along with recent examples that demonstrate how these factors affect the printing process.

A variety of features, including high-aspect pillars, hollow parts, and overhangs that otherwise are difficult to fabricate at a small scale, can now be integrated within single objects using AM. Clearly, further advances in the field require combined multidisciplinary efforts to impact the technology, mainly in terms of improved resolution and speed/throughput, as well as chemistry and materials. The cutting-edge aspect of the e-AM technologies is a multimaterial capacity to enable a new degree of freedom in microfabrication of complex designs. Thus, 3D printing promises to advance a variety of future technologies at the micro- and nanoscale, from microrobotics and sensing, catalytic interfaces, advanced memory devices, and quantum systems.

DISCLOSURE STATEMENT

The authors are not aware of any affiliations, memberships, funding, or financial holdings that might be perceived as affecting the objectivity of this review.

ACKNOWLEDGMENTS

LITERATURE CITED

1. Loterie D, Delrot P, Moser C. 2020. High-resolution tomographic volumetric additive manufacturing. *Nat. Commun.* 11:852
2. Gibson I, Rosen D, Stucker B. 2015. *Additive Manufacturing Technologies: 3D Printing, Rapid Prototyping, and Direct Digital Manufacturing*. New York: Springer
3. Aejmelaeus-Lindström P, Rusenova G, Mirjan A, Medina Ibáñez J, Gramazio F, Kohler M. 2020. Rock print pavilion: robotically fabricating architecture from rock and string. *Constr. Robot.* 4:97–113
4. Sturmer J. 2015. 3D printing: Australian researchers create jet engine, breakthrough captures attention of Airbus and Boeing. *ABC News*, Feb. 25. **https://www.abc.net.au/news/2015-02-26/australian-researchers-create-first-3d-jet-engine/6262462**
5. LaFratta CN, Fourkas JT, Baldacchini T, Farrer RA. 2007. Multiphoton fabrication. *Angew. Chem. Int. Ed.* 46:6238–58
6. Fischer J, Wegener M. 2013. Three-dimensional optical laser lithography beyond the diffraction limit. *Laser Photon. Rev.* 7:22–44
7. Stampfl J, Liska R, Ovsianikov A. 2016. *Multiphoton Lithography: Techniques, Materials, and Applications*. Weinheim, Ger.: Wiley-VCH Verlag
8. Lamont AC, Restaino MA, Kim MJ, Sochol RD. 2019. A facile multi-material direct laser writing strategy. *Lab Chip* 19:2340–45
9. Pearre BW, Michas C, Tsang JM, Gardner TJ, Otchy TM. 2019. Fast micron-scale 3D printing with a resonant-scanning two-photon microscope. *Addit. Manuf.* 30:100887
10. Hahn V, Messer T, Bojanowski NM, Curticean ER, Wacker I, et al. 2021. Two-step absorption instead of two-photon absorption in 3D nanoprinting. *Nat. Photon.* 15:932–38
11. Geng Q, Wang D, Chen P, Chen SC. 2019. Ultrafast multi-focus 3-D nano-fabrication based on two-photon polymerization. *Nat. Commun.* 10:2179

12. Yang L, Hu H, Scholz A, Feist F, Cadilha Marques G, et al. 2023. Laser printed microelectronics. *Nat. Commun.* 14:1103

13. Gamburg YD, Zangari G. 2011. *Theory and Practice of Metal Electrodeposition*. New York: Springer

14. Ansari R. 2006. Polypyrrole conducting electroactive polymers: synthesis and stability studies. *E-J. Chem.* 3:860413

15. Kim S, Jang LK, Park HS, Lee JY. 2016. Electrochemical deposition of conductive and adhesive polypyrrole-dopamine films. *Sci. Rep.* 6:30475

16. Akbulut H, Yavuz M, Guler E, Demirkol DO, Endo T, et al. 2014. Electrochemical deposition of polypeptides: bio-based covering materials for surface design. *Polym. Chem.* 5:3929–36

17. Ammam M. 2014. Electrochemical and electrophoretic deposition of enzymes: principles, differences and application in miniaturized biosensor and biofuel cell electrodes. *Biosensors Bioelectron.* 58:121–31

18. Rodolfa KT, Bruckbauer A, Zhou D, Korchev YE, Klenerman D. 2005. Two-component graded deposition of biomolecules with a double-barreled nanopipette. *Angew. Chem. Int. Ed.* 44:6854–59

19. Zhang Z, Kitada A, Fukami K, Yao Z, Murase K. 2020. Electrodeposition of an iron thin film with compact and smooth morphology using an ethereal electrolyte. *Electrochim. Acta* 348:136289

20. Luo B, Yang D, Liang M, Zhi L. 2010. Large-scale fabrication of single crystalline tin nanowire arrays. *Nanoscale* 2:1661–64

21. Tonelli D, Scavetta E, Gualandi I. 2019. Electrochemical deposition of nanomaterials for electrochemical sensing. *Sensors* 19:1186

22. Jabbar A, Yasin G, Khan WQ, Anwar MY, Korai RM, et al. 2017. Electrochemical deposition of nickel graphene composite coatings: effect of deposition temperature on its surface morphology and corrosion resistance. *RSC Adv.* 7:31100–9

23. Liu A, Li C, Bai H, Shi G. 2010. Electrochemical deposition of polypyrrole/sulfonated graphene composite films. *J. Phys. Chem. C* 114:22783–89

24. Hengsteler J, Mandal B, van Nisselroy C, Lau GPS, Schlotter T, et al. 2021. Bringing electrochemical three-dimensional printing to the nanoscale. *Nano Lett.* 21:9093–101

25. Ercolano G, Zambelli T, van Nisselroy C, Momotenko D, Vörös J, et al. 2020. Multiscale additive manufacturing of metal microstructures. *Adv. Eng. Mater.* 22:1900961

26. Reiser A, Linden M, Rohner P, Marchand A, Galinski H, et al. 2019. Multi-metal electrohydrodynamic redox 3D printing at the submicron scale. *Nat. Commun.* 10:1853

27. Ercolano G, van Nisselroy C, Merle T, Vörös J, Momotenko D, et al. 2020. Additive manufacturing of sub-micron to sub-mm metal structures with hollow AFM cantilevers. *Micromachines* 11:11010006

28. Park Y-G, Yun I, Chung WG, Park W, Lee DH, Park J-U. 2022. High-resolution 3D printing for electronics. *Adv. Sci.* 9:2104623

29. Hengsteler J, Lau GPS, Zambelli T, Momotenko D. 2021. Electrochemical 3D micro- and nanoprinting: current state and future perspective. *Electrochem. Sci. Adv.* 2:e2100123

30. Hirt L, Reiser A, Spolenak R, Zambelli T. 2017. Additive manufacturing of metal structures at the micrometer scale. *Adv. Mater.* 29:1604211

31. Je JH, Kim JM, Jaworski J. 2017. Progression in the fountain pen approach: from 2D writing to 3D free-form micro/nanofabrication. *Small* 13:1600137

32. Hirt L, Grüter RR, Berthelot T, Cornut R, Vörös J, Zambelli T. 2015. Local surface modification via confined electrochemical deposition with FluidFM. *RSC Adv.* 5:84517–22

33. Hirt L, Ihle S, Pan Z, Dorwling-Carter L, Reiser A, et al. 2016. Template-free 3D microprinting of metals using a force-controlled nanopipette for layer-by-layer electrodeposition. *Adv. Mater.* 28:2311–15

34. Meister A, Gabi M, Behr P, Studer P, Vörös J, et al. 2009. FluidFM: combining atomic force microscopy and nanofluidics in a universal liquid delivery system for single cell applications and beyond. *Nano Lett.* 9:2501–7

35. Hansma PK, Drake B, Marti O, Gould SAC, Prater CB. 1989. The scanning ion-conductance microscope. *Science* 243:641–43

36. Momotenko D, Page A, Adobes-Vidal M, Unwin PR. 2016. Write–read 3D patterning with a dual-channel nanopipette. *ACS Nano* 10:8871–78

37. Nakazawa K, Yoshioka M, Mizutani Y, Ushiki T, Iwata F. 2020. Local electroplating deposition for free-standing micropillars using a bias-modulated scanning ion conductance microscope. *Microsyst. Technol.* 26:1333–42

38. Hu J, Yu M-F. 2010. Meniscus-confined three-dimensional electrodeposition for direct writing of wire bonds. *Science* 329:313–16

39. Daryadel S, Behroozfar A, Morsali SR, Moreno S, Baniasadi M, et al. 2018. Localized pulsed electrodeposition process for three-dimensional printing of nanotwinned metallic nanostructures. *Nano Lett.* 18:208–14

40. Chen X, Liu X, Ouyang M, Chen J, Taiwo O, et al. 2019. Multi-metal 4D printing with a desktop electrochemical 3D printer. *Sci. Rep.* 9:3973

41. Ejjigu N, Abdelgadir K, Flaten Z, Hoff C, Li C-Z, Sun D. 2022. Environmental noise reduction for tunable resistive pulse sensing of extracellular vesicles. *Sens. Actuators A* 346:113832

42. Gao R, Edwards MA, Harris JM, White HS. 2020. Shot noise sets the limit of quantification in electrochemical measurements. *Curr. Opin. Electrochem.* 22:170–77

43. Guillaume-Gentil O, Potthoff E, Ossola D, Franz CM, Zambelli T, Vorholt JA. 2014. Force-controlled manipulation of single cells: from AFM to FluidFM. *Trends Biotechnol.* 32:381–88

44. Aramesh M, Forró C, Dorwling-Carter L, Lüchtefeld I, Schlotter T, et al. 2019. Localized detection of ions and biomolecules with a force-controlled scanning nanopore microscope. *Nat. Nanotechnol.* 14:791–98

45. Chen M, Xu Z, Kim JH, Seol SK, Kim JT. 2018. Meniscus-on-demand parallel 3D nanoprinting. *ACS Nano* 12:4172–77

46. Nadappuram BP, McKelvey K, Byers JC, Güell AG, Colburn AW, et al. 2015. Quad-barrel multifunctional electrochemical and ion conductance probe for voltammetric analysis and imaging. *Anal. Chem.* 87:3566–73

47. Yeshua T, Layani M, Dekhter R, Huebner U, Magdassi S, Lewis A. 2018. Micrometer to 15 nm printing of metallic inks with fountain pen nanolithography. *Small* 14:1702324

48. Liao H-S, Werner C, Slipets R, Larsen PE, Hwang I-S, et al. 2022. Low-cost, open-source XYZ nanopositioner for high-precision analytical applications. *HardwareX* 11:e00317

49. Minase J, Lu TF, Cazzolato B, Grainger S. 2010. A review, supported by experimental results, of voltage, charge and capacitor insertion method for driving piezoelectric actuators. *Precis. Eng.* 34:692–700

50. Ronkanen P, Kallio P, Vilkko M, Koivo HN. 2011. Displacement control of piezoelectric actuators using current and voltage. *IEEE/ASME Trans. Mechatron.* 16:160–66

51. McKelvey K, Perry D, Byers JC, Colburn AW, Unwin PR. 2014. Bias modulated scanning ion conductance microscopy. *Anal. Chem.* 86:3639–46

52. Zhu C, Huang K, Siepser NP, Baker LA. 2021. Scanning ion conductance microscopy. *Chem. Rev.* 121:11726–68

53. Eliyahu D, Gileadi E, Galun E, Eliaz N. 2020. Atomic force microscope-based meniscus-confined three-dimensional electrodeposition. *Adv. Mater. Technol.* 5:1900827

54. Lin Y-P, Zhang Y, Yu M-F. 2019. Parallel process 3D metal microprinting. *Adv. Mater. Technol.* 4:1800393

55. Galliker P, Schneider J, Eghlidi H, Kress S, Sandoghdar V, Poulikakos D. 2012. Direct printing of nanostructures by electrostatic autofocussing of ink nanodroplets. *Nat. Commun.* 3:890

56. Reiser A. 2019. *Additive manufacturing of metals at small length scales—microstructure, properties and novel multi-metal electrochemical concepts*. Doctoral Thesis, ETH Zurich, Switz.

57. Guillaume-Gentil O, Grindberg RV, Kooger R, Dorwling-Carter L, Martinez V, et al. 2016. Tunable single-cell extraction for molecular analyses. *Cell* 166:506–16

58. Tritton DJ. 1988. *Physical Fluid Dynamics*. New York: Oxford Univ. Press. 2nd ed.

59. Yamada J, Matsuda H. 1973. Limiting diffusion currents in hydrodynamic voltammetry: III. Wall jet electrodes. *J. Electroanal. Chem. Interfacial Electrochem.* 44:189–98

60. Momotenko D, Byers JC, McKelvey K, Kang M, Unwin PR. 2015. High-speed electrochemical imaging. *ACS Nano* 9:8942–52

61. Lomax DJ, Kant P, Williams AT, Patten HV, Zou Y, et al. 2016. Ultra-low voltage electrowetting using graphite surfaces. *Soft Matter* 12:8798–804

62. Lei Y, Zhang X, Xu D, Yu M, Yi Z, et al. 2018. Dynamic "scanning-mode" meniscus confined electrode-positing and micropatterning of individually addressable ultraconductive copper line arrays. *J. Phys. Chem. Lett.* 9:2380–87

63. Lei Y, Zhang X, Nie W, Zhang Y, Gao Q, et al. 2021. The composition and magnetic property of Co/Cu alloy microwires prepared using meniscus-confined electrodeposition: effect of $[Co^{2+}]$, $[Cu^{2+}]$ concentration at the tip of the meniscus. *J. Electrochem. Soc.* 168:112507

64. Seol SK, Kim D, Lee S, Kim JH, Chang WS, Kim JT. 2015. Electrodeposition-based 3D printing of metallic microarchitectures with controlled internal structures. *Small* 11:3896–902

65. Persad AH, Ward CA. 2016. Expressions for the evaporation and condensation coefficients in the Hertz-Knudsen relation. *Chem. Rev.* 116:7727–67

66. Morsali S, Daryadel S, Zhou Z, Behroozfar A, Baniasadi M, et al. 2017. Multi-physics simulation of metal printing at micro/nanoscale using meniscus-confined electrodeposition: effect of nozzle speed and diameter. *J. Appl. Phys.* 121:214305

67. Morsali S, Daryadel S, Zhou Z, Behroozfar A, Qian D, Minary-Jolandan M. 2017. Multi-physics simulation of metal printing at micro/nanoscale using meniscus-confined electrodeposition: effect of environmental humidity. *J. Appl. Phys.* 121:024903

68. Li Y, Chen H, Xiao S, Alibakhshi MA, Lo C-W, et al. 2019. Ultrafast diameter-dependent water evaporation from nanopores. *ACS Nano* 13:3363–72

69. Mkhize N, Bhaskaran H. 2022. Electrohydrodynamic jet printing: Introductory concepts and considerations. *Small Sci.* 2:2100073

70. Chen CH, Saville DA, Aksay IA. 2006. Scaling laws for pulsed electrohydrodynamic drop formation. *Appl. Phys. Lett.* 89:124103

71. Lindén M. 2017. *Merging electrohydrodynamic printing and electrochemistry: sub-micronscale 3D-printing of metals*. Master's Thesis, Uppsala Univ., Sweden

72. Reiser A, Koch L, Dunn KA, Matsuura T, Iwata F, et al. 2020. Metals by micro-scale additive manufacturing: comparison of microstructure and mechanical properties. *Adv. Funct. Mater.* 30:1910491

73. van Nisselroy C, Shen C, Zambelli T, Momotenko D. 2022. Electrochemical 3D printing of silver and nickel microstructures with FluidFM. *Addit. Manuf.* 53:102718

74. Menetrey M, Koch L, Sologubenko A, Gerstl S, Spolenak R, Reiser A. 2022. Targeted additive micromodulation of grain size in nanocrystalline copper nanostructures by electrohydrodynamic redox 3D printing. *Small* 18:2205302

75. Behroozfar A, Daryadel S, Morsali SR, Moreno S, Baniasadi M, et al. 2018. Microscale 3D printing of nanotwinned copper. *Adv. Mater.* 30:1705107

76. Zhang X, Yuan L, Lei Y, Zhang Y, Li Y, et al. 2021. Electrochemical gradients driven 3D printing of nano-twinned copper structures by direct current dynamic meniscus confined electrodeposition. *Appl. Mater. Today* 24:101138

77. Ramachandramoorthy R, Kalácska S, Poras G, Schwiedrzik J, Edwards TEJ, et al. 2022. Anomalous high strain rate compressive behavior of additively manufactured copper micropillars. *Appl. Mater. Today* 27:101415

78. Suryavanshi AP, Yu M-F. 2007. Electrochemical fountain pen nanofabrication of vertically grown platinum nanowires. *Nanotechnology* 18:105305

79. Wang C, Hossain Bhuiyan ME, Moreno S, Minary-Jolandan M. 2020. Direct-write printing copper–nickel (Cu/Ni) alloy with controlled composition from a single electrolyte using co-electrodeposition. *ACS Appl. Mater. Interfaces* 12:18683–91

80. Shen C, Zhu Z, Zhu D, van Nisselroy C, Zambelli T, Momotenko D. 2022. Electrochemical 3D printing of Ni–Mn and Ni–Co alloy with FluidFM. *Nanotechnology* 33:265301

81. McKelvey K, O'Connell MA, Unwin PR. 2013. Meniscus confined fabrication of multidimensional conducting polymer nanostructures with scanning electrochemical cell microscopy (SECCM). *Chem. Commun.* 49:2986–88

82. Kim JT, Seol SK, Pyo J, Lee JS, Je JH, Margaritondo G. 2011. Three-dimensional writing of conducting polymer nanowire arrays by meniscus-guided polymerization. *Adv. Mater.* 23:1968–70

83. Zhang P, Aydemir N, Alkaisi M, Williams DE, Travas-Sejdic J. 2018. Direct writing and characterization of three-dimensional conducting polymer PEDOT arrays. *ACS Appl. Mater. Interfaces* 10:11888–95

84. Tomaskovic-Crook E, Zhang P, Ahtiainen A, Kaisvuo H, Lee CY, et al. 2019. Human neural tissues from neural stem cells using conductive biogel and printed polymer microelectrode arrays for 3D electrical stimulation. *Adv. Healthc. Mater.* 8:1900425

85. Won KH, Weon BM, Je JH. 2013. Polymer composite microtube array produced by meniscus-guided approach. *AIP Adv.* 3:092127

86. Ventrici de Souza J, Liu Y, Wang S, Dorig P, Kuhl TL, et al. 2018. Three-dimensional nanoprinting via direct delivery. *J. Phys. Chem. B* 122:956–62

87. Pattison TG, Wang S, Miller RD, Liu GY, Qiao GG. 2022. 3D nanoprinting via spatially controlled assembly and polymerization. *Nat. Commun.* 13:1941

88. Liu Y, Yang J, Tao C, Lee H, Chen M, et al. 2022. Meniscus-guided 3D microprinting of pure metal-organic frameworks with high gas-uptake performance. *ACS Appl. Mater. Interfaces* 14:7184–91

89. Chen M, Hu S, Zhou Z, Huang N, Lee S, et al. 2021. Three-dimensional perovskite nanopixels for ultrahigh-resolution color displays and multilevel anticounterfeiting. *Nano Lett.* 21:5186–94

90. Chen M, Yang J, Wang Z, Xu Z, Lee H, et al. 2019. 3D nanoprinting of perovskites. *Adv. Mater.* 31:e1904073

91. Lee J, Oh S, Pyo J, Kim JM, Je JH. 2015. A light-driven supramolecular nanowire actuator. *Nanoscale* 7:6457–61

92. Oh S, Kwak EA, Jeon S, Ahn S, Kim JM, Jaworski J. 2014. Responsive 3D microstructures from virus building blocks. *Adv. Mater.* 26:5217–22

93. Onses MS, Sutanto E, Ferreira PM, Alleyne AG, Rogers JA. 2015. Mechanisms, capabilities, and applications of high-resolution electrohydrodynamic jet printing. *Small* 11:4237–66

94. Meng Z, Li J, Chen Y, Gao T, Yu K, et al. 2022. Micro/nanoscale electrohydrodynamic printing for functional metallic structures. *Mater. Today Nano* 20:100254

95. Klein F, Richter B, Striebel T, Franz CM, von Freymann G, et al. 2011. Two-component polymer scaffolds for controlled three-dimensional cell culture. *Adv. Mater.* 23:1341–45

96. Doherty RP, Varkevisser T, Teunisse M, Hoecht J, Ketzetzi S, et al. 2020. Catalytically propelled 3D printed colloidal microswimmers. *Soft Matter* 16:10463–69

97. Bunea A-I, del Castillo Iniesta N, Droumpali A, Wetzel AE, Engay E, Taboryski R. 2021. Micro 3D printing by two-photon polymerization: configurations and parameters for the nanoscribe system. *Micro* 1:164–80

98. Bae J, Lee S, Ahn J, Kim JH, Wajahat M, et al. 2020. 3D-printed quantum dot nanopixels. *ACS Nano* 14:10993–1001